Velocity fluctuations and boundary layer structure in a rough Rayleigh-Bénard cell filled with water

Olivier Liot,[*] Quentin Ehlinger,[†] Éléonore Rusaouën,[‡] Thibaut Coudarchet, Julien Salort, and Francesca Chillà[§]

Univ Lyon, ENS de Lyon, Univ Claude Bernard, CNRS, Laboratoire de Physique, F-69342 Lyon Cedex 7, France

(Received 3 November 2016; published 26 April 2017)

We report particle image velocimetry of the large-scale circulation and the viscous boundary layer in turbulent thermal convection. We use two parallelepipedic Rayleigh-Bénard cells with a top smooth plate. The first one has a rough bottom plate and the second one has a smooth one, so we compare the rough-smooth and the smooth-smooth configurations. The dimensions of the cell allow us to consider a bidimensional mean flow. Many previous heat flux measurements have shown a Nusselt-Rayleigh regime transition corresponding to an increase of the heat flux in the presence of roughness that is higher than the surface increase. Our velocity measurements show that if the mean velocity field is not clearly affected by the roughness, the velocity fluctuations rise dramatically, which is accompanied by a change of the longitudinal velocity structure functions scaling. Moreover, we show that the boundary layer becomes turbulent close to roughness, as it was observed recently in air [O. Liot *et al.*, J. Fluid Mech. **786**, 275 (2016)]. Finally, we discuss the link between the change of the boundary layer structure and the changes observed in the velocity fluctuations.

DOI: 10.1103/PhysRevFluids.2.044605

I. INTRODUCTION

Buoyancy fluctuations are the engine of various flows. Atmospheric circulation or earth's mantle motions are governed by thermal convection. Many industrial applications (cooling of a nuclear plant, for example) also use this kind of flow. Because thermal convection is often turbulent, it is a very efficient way for carrying heat. However, even though this flow is very accessible and has been studied for a long time [1,2], many properties and mechanisms in play in turbulent thermal convection still need to be understood. In the laboratory, we have chosen to model thermal convection flows with the Rayleigh-Bénard configuration: a horizontal layer of fluid confined between a cooling plate above and a heating plate below. The Rayleigh number measures the forcing due to buoyancy effects compared to dissipative ones:

$$\mathrm{Ra} = \frac{g\alpha\Delta T H^3}{\nu\kappa}, \tag{1}$$

where H is the height of the cell, g is the acceleration due to gravity, α is the constant pressure thermal expansion coefficient of the fluid, ν is its kinematic viscosity, κ is its thermal diffusivity, and $\Delta T = T_h - T_c$ is the difference in temperature between the heating and cooling plates. The Prandtl

[*]Present address: LAAS-CNRS, 7 Avenue du Colonel Roche, 31400 Toulouse, France, EU.

[†]Present address: Univ Lyon, Université Claude Bernard Lyon 1, CNRS, Institut Lumière Matière, Campus LyonTech-La Doua, Bâtiment Kastler, 10 Rue Ada Byron, 69622 Villeurbanne Cedex, France, EU.

[‡]Present address: LEGI, Domaine Universitaire, CS 40700, 38058 Grenoble Cedex 9, France, EU.

[§]francesca.chilla@ens-lyon.fr

number compares viscosity to thermal diffusivity:

$$\mathrm{Pr} = \frac{\nu}{\kappa}. \tag{2}$$

The last standard parameter is the aspect ratio Γ, which is the ratio between the characteristic transverse length of the cell and its height H. These numbers represent the control parameters of thermal convection. We represent the response of the system by the dimensionless heat flux, the Nusselt number

$$\mathrm{Nu} = \frac{QH}{\lambda \Delta T}, \tag{3}$$

where Q is the global heat flux and λ is the thermal conductivity of the fluid.

In turbulent Rayleigh-Bénard convection, the mixing makes the bulk temperature almost homogeneous. Temperature gradients are confined close to the plates in thermal boundary layers. Their thickness can be computed by

$$\delta_{\mathrm{th}} = \frac{H}{2\,\mathrm{Nu}}. \tag{4}$$

Viscous boundary layers also develop along the plates. Thermal transfer is due to interactions between the bulk and these boundary layers. In particular, plumes are slices of layers that detach and go towards the opposite plate. They play a crucial role in thermal transfer [3] and understanding their statistics, structure, and coherence is still a challenge [4].

Some progress was made in the understanding of the relation between response and control parameters. In particular, much effort has concentrated on the study of the relation between thermal forcing and heat flux $\mathrm{Nu} \propto \mathrm{Ra}^{\gamma}$ [5–8]. Nevertheless, alternative methods are necessary to have a larger scope of turbulent Rayleigh-Bénard convection [4].

One such method, used in the present paper, consists in a destabilization of the boundary layers with controlled roughness. Tong, Xia and co-workers used pyramid-shaped roughness on both plates [9–11]. They observed a heat flux enhancement up to 76% compared to a smooth case, which is higher than the surface increase, even if there is not always a change for the scaling exponent γ. This enhancement is attributed to an increase of the plumes emission by the top of roughness. This result can be extended to cells where only one plate is rough [12]. Groove-shaped roughness was used by Roche *et al.* [13] and the scaling exponent reached $\gamma = 1/2$. Numerical simulations for the same geometry showed an increase of γ too [14]. An increase of the scaling exponent was also observed by Ciliberto and Laroche [15] with randomly distributed glass spheres on the bottom plate. All these observations put forward that the heat flux enhancement relative to a smooth configuration starts from a transitional Rayleigh number Ra_t. It is now admitted that the Nu-Ra regime transition appears when the thermal boundary layer thickness becomes similar to the roughness height h_0 [16]. The corresponding transition Nusselt number is

$$\mathrm{Nu}_t = \frac{H}{2h_0}. \tag{5}$$

Several experiments have been performed with square-stud roughness on the bottom plate, in both a cylindrical cell [16] and a parallelepipedic cell [17] filled with water. Similar results about the heat flux increase have been observed. Moreover, very close to roughness, the study of temperature fluctuations has led us to a phenomenological model based on a destabilization of the boundary layer. This model is in good agreement with global heat flux measurements. This destabilization was confirmed by velocity measurements inside the viscous boundary layer close to roughness in a proportional cell filled with air. These experiments showed that the viscous boundary layer transits to a turbulent state above roughness [18].

Box-shaped roughness has been studied analytically [19] and numerically [20]. It consists in four elements on the bottom plate whose height is much larger than the thermal boundary layer thickness. It is different from previous studies where the roughness and thermal boundary layer have a similar

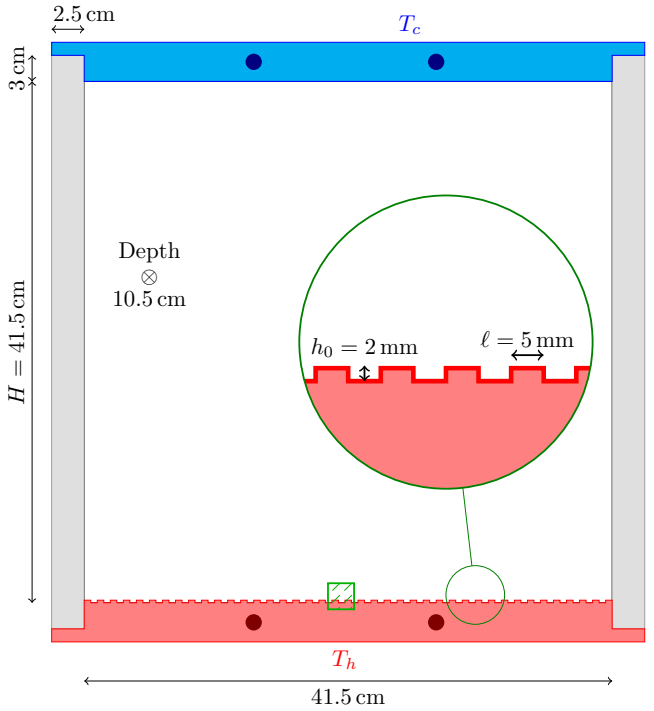

FIG. 1. Sketch of the RS convection cell. The four dark circles in the plates show the locations of the PT100 temperature sensors. The close-up shows the roughness dimensions. Particle image velocimetry measurements of the viscous boundary layer are performed in the green hatched area.

size. An increase in γ is observed and then a saturation of the supplementary heat flux rise occurs when the zones between the roughness elements are totally washed out by the fluid.

In this paper we present particle image velocimetry (PIV) measurements performed in the whole cell and close to roughness. We used the same cell as Salort *et al.* [17]. The bottom plate is rough whereas the top one is smooth. A similar cell is used with both smooth plates for comparison. Whereas no effect on the mean velocity field is clearly visible, a large increase of the velocity fluctuations is observed with the presence of roughness, probably related to an increase of plumes emission and intensity. This is accompanied by a change of the shape of the velocity structure function. Moreover, hints of logarithmic velocity profiles are put forward above roughness in the same way as a previous study in the air [18], which is evidence of the transition to turbulence of the viscous boundary layer. We recall that logarithmic temperature profiles have already been observed close to smooth plates [21]. They can appear without logarithmic velocity profiles.

II. EXPERIMENTAL SETUP AND PIV ACQUISITION

The section presents the experimental setup and the velocity acquisition method.

A. Convection cells

We use a 10.5-cm-thick parallelepipedic convection cell of 41.5×41.5 cm^2 with 2.5-cm-thick poly(methyl methacrylate) walls (see sketch in Fig. 1). The top plate consists of a 4-cm-thick copper plate coated with a thin layer of nickel. The bottom plate is an aluminium alloy (5083) anodized in black. It is Joule heated while the top plate is cooled with temperature-regulated water circulation. Plate temperatures are measured by PT100 temperature sensors. On the bottom plate, periodic

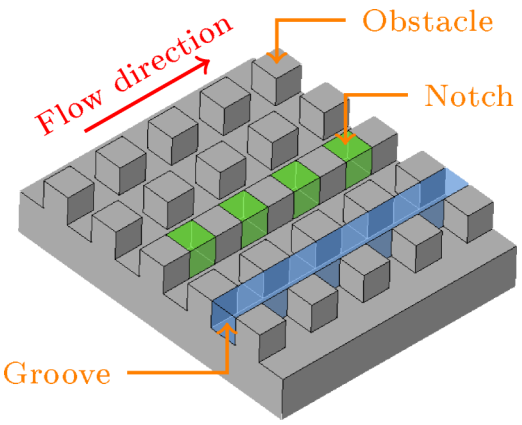

FIG. 2. Detail of roughness with the three different locations according to the flow direction.

roughness is machined directly in the plate. It consists of an array of 0.2-cm-high, 0.5×0.5 cm^2 square obstacles (close-up in Fig. 1). Because of the cell dimensions, we can assume that the mean flow is quasibidimensional. Thus, according to the flow direction, we can distinguish three positions close to roughness: above an obstacle, inside a notch where the fluid is "protected" from the mean flow, and in the groove between obstacle rows (Fig. 2). We refer to this as a rough-smooth (RS) cell. Moreover, we use a very similar cell with a smooth bottom plate to perform reference global velocity measurements. The only difference is that the bottom plate is in copper anodized with a thin layer of nickel. This is referred to as a smooth-smooth (SS) cell.

The cells are filled with deionized water. The main experimental parameters are grouped in Table I. The regime transition (i.e., when the heat flux in the RS configuration becomes higher than in the SS one) occurs when the thermal boundary layer reaches h_0. We have $\mathrm{Nu}_t = H/2h_0$ according to Eq. (5). If we suppose in this cell the relation $\mathrm{Nu} = 0.06\,\mathrm{Ra}^{1/3}$ [17], the Nusselt-Rayleigh regime transition occurs for $\mathrm{Ra}_t = 4.1 \times 10^9$. Consequently, we work at a Rayleigh number far after the transition. Concerning the velocity measurements close to roughness, Table II sums up the experimental conditions. Unfortunately, in this cell we are not able to reach Rayleigh numbers below the transition threshold while allowing visualization and stable flow.

B. Particle image velocimetry acquisition

Particle image velocimetry acquisitions are performed using a 1.2-W, Nd:YVO_4 laser. With a cylindrical lens we build a vertical laser sheet that enters the cell from the observer's left-hand side. We seed the flow with Sphericel 110P8 glass beads with a density of 1.10 ± 0.05 and 12 μm average diameter.

For global velocity field acquisitions we use a digital camera Stingray F-125B. We perform 12-hour acquisitions with one picture pair every 10 s (4320 picture pairs). Pictures of the same pair are separated by 50 ms. For analysis we use the free software CIVX [22]. For the RS plate, we use a first pass of picture pair cross correlation with 64×64 pixels^2 boxes with 50% overlap.

TABLE I. Parameters used for the global velocity measurements in the RS and SS cells.

Cell	ΔT	$T_m = (T_h + T_b)/2$	Ra	Pr
RS	25.9 °C	40.0 °C	7.0×10^{10}	4.4
SS	25.7 °C	40.0 °C	6.9×10^{10}	4.4

TABLE II. Experimental parameters used for the velocity measurements close to roughness.

ΔT	$T_m = (T_h + T_b)/2$	Ra	Pr
14.8 °C	40.0 °C	4.0×10^{10}	4.4

Search boxes are one and a half times larger. Then other passes are used with smaller boxes. For the SS cell, we use the same method but with a first pass box size of 30×30 pixels^2. The resulting resolution gets down to about 3 mm in the RS cell and 6 mm in the SS one. For measurements close to roughness, a faster acquisition process is necessary to have sufficient space and time resolution for the PIV treatment. We use a IOI Flare 2M360CL digital camera. Pictures are captured continuously at frequencies from 200 to 340 frames per second. The resolution gets down to about 250 μm. Acquisitions are performed, on the one hand, in a groove and, on the other hand, above obstacles and in notches simultaneously. All of these locations are chosen at the center of the cell (see Fig. 1).

III. STUDY OF LARGE-SCALE CIRCULATION

This section consists in observing global velocity fields, velocity fluctuations, and velocity longitudinal structure functions in the whole cell. We compare the RS and SS cells.

A. Mean velocity fields

First of all, we plot the mean velocity magnitude map. Figure 3 compares the RS case to the SS one. We proceed at close Rayleigh numbers, $\mathrm{Ra} = 7.0 \times 10^{10}$ and $\mathrm{Ra} = 6.9 \times 10^{10}$, respectively, which allows a direct comparison of the measurements. In both cases we choose acquisitions where the large-scale circulation (LSC) occurs counterclockwise. Hot and cold jets spread along the right and left sidewalls, respectively. Corresponding velocities are around 2.2 cm/s, whereas in the central part of the flows, the velocity magnitude is quite slower (∼0.5 cm/s). The SS velocity field is very similar to that obtained by Xia *et al.* [23] in a proportional cell filled with water for $\mathrm{Ra} = 3.5 \times 10^{10}$. We observe that the LSC structure is very similar for both RS and SS cells. Nevertheless, the velocity in the hot jet seems a little bit higher for the RS case. The mean velocity in the SS cell is 1.36 ± 0.01 cm/s, versus 1.43 ± 0.01 cm/s in the RS cell, which corresponds to a 5% increase. If

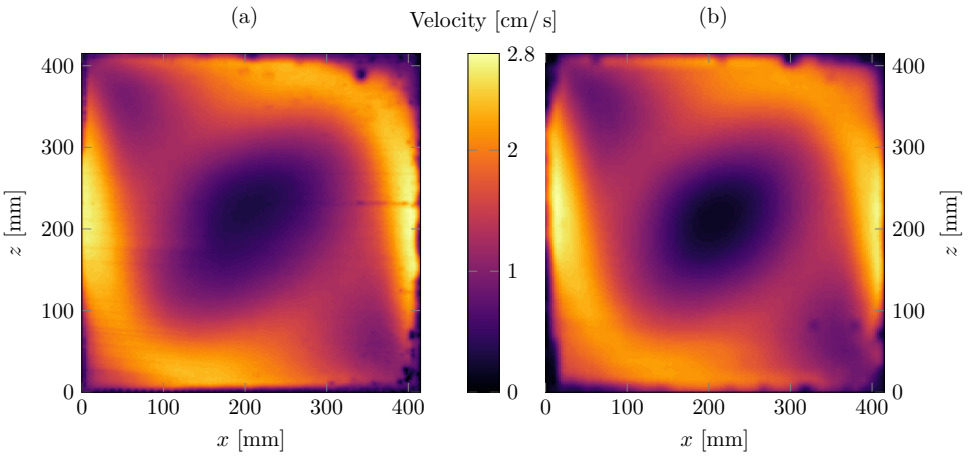

FIG. 3. Velocity magnitude fields in (a) the RS cell for $\mathrm{Ra} = 7.0 \times 10^{10}$ and (b) the SS cell for $\mathrm{Ra} = 6.9 \times 10^{10}$.

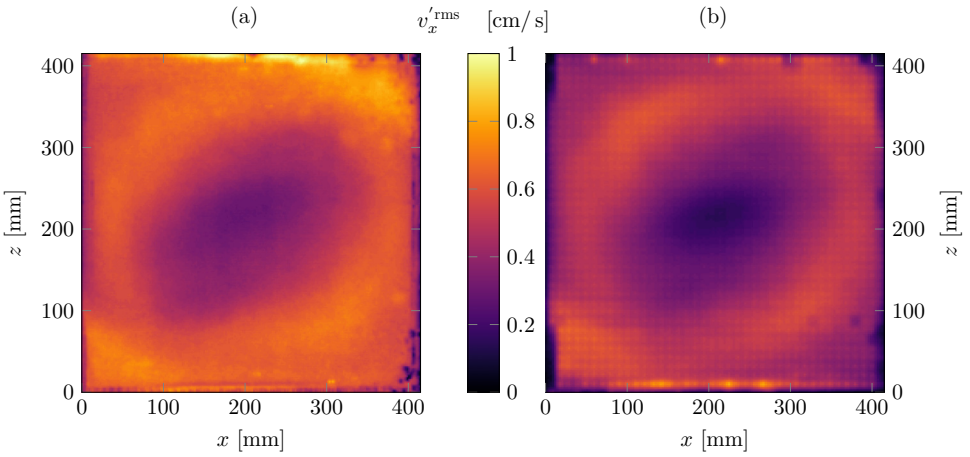

FIG. 4. Horizontal velocity fluctuation rms field in (a) the RS cells for $\mathrm{Ra} = 7.0 \times 10^{10}$ and (b) the SS cells for $\mathrm{Ra} = 6.9 \times 10^{10}$, with counterclockwise LSC.

it is not a large difference, there is a possible effect of roughness because the Rayleigh number for the RS case is only 1.5% higher than for the SS one, which corresponds to a negligible Reynolds number increase of about 1%. This observation lets us think that there is a small effect of roughness on the mean velocity field. However, this small velocity difference may fall within the experimental uncertainties due to parallax, i.e., calibration of laser sheet orientation.

B. Velocity fluctuations

Because we do not see a clear influence of roughness on the mean velocity fields, we try to observe it on the velocity fluctuations. We compute the velocity fluctuations root mean square (rms) for the horizontal (v_x') and vertical (v_z') velocity fluctuations as

$$v_i'^{\mathrm{rms}}(x,z) = \sqrt{\langle [v_i(x,z,t) - \langle v_i(x,z,t)\rangle_t]^2\rangle_t}, \tag{6}$$

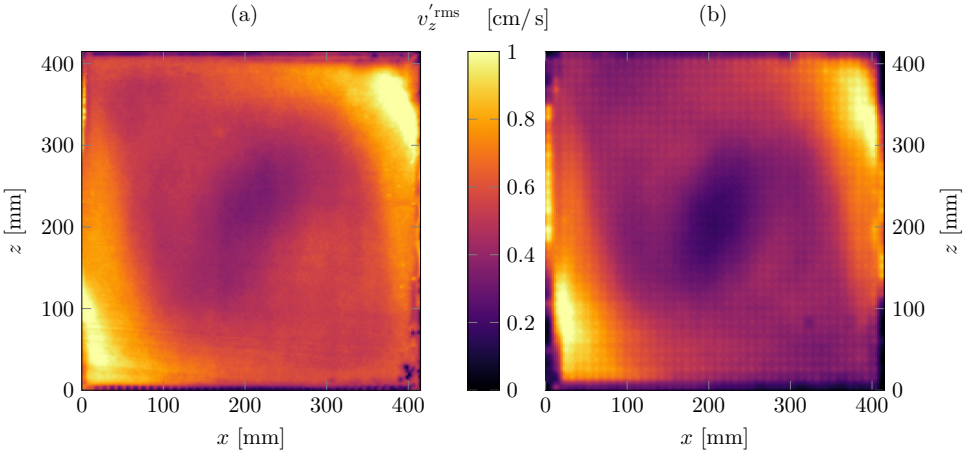

FIG. 5. Vertical velocity fluctuations rms field in (a) the RS cells for $\mathrm{Ra} = 7.0 \times 10^{10}$ and (b) the SS cells for $\mathrm{Ra} = 6.9 \times 10^{10}$, with counterclockwise LSC.

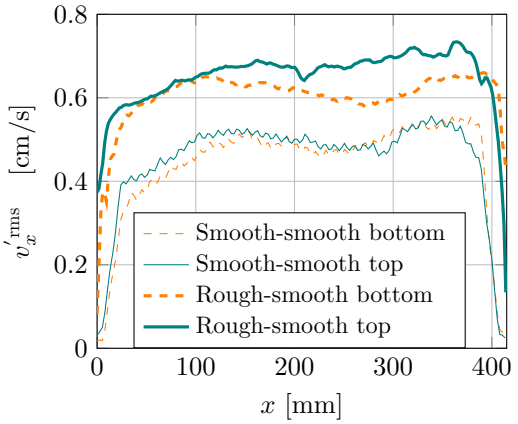

FIG. 6. Profiles of average fields of horizontal velocity rms. Profiles of the bottom region are horizontally flipped for a better comparison. Statistical uncertainties do not exceed 0.02 cm/s. For more details about calculations, see the text.

where $i = x,z$. With this definition, we report in Figs. 4 and 5 the rms values of the horizontal and vertical components, respectively. Figures 4(a) and 5(a) are for the RS configuration and Figs. 4(b) and 5(b) for the SS one.

The most remarkable fact concerns the larger fluctuation intensity in the RS cell compared to the SS one. The average horizontal velocity fluctuation rms is 0.43 ± 0.01 cm/s in the SS cell and 0.56 ± 0.01 cm/s in the RS one. This corresponds to a 30% increase. We observe a similar change for the vertical velocity fluctuations rms with a 23% increase (from 0.47 ± 0.01 cm/s to 0.58 ± 0.01 cm/s). These fluctuations may originate from the destabilization of the thermal boundary layers by roughness observed by Salort *et al.* [17] and the pending transition to turbulence of the viscous boundary layer [18]. This destabilization induces probably an increase of plume emission and/or intensity, which leads to a crucial increase of the velocity fluctuations.

The spatial structure of the horizontal velocity fluctuation rms field for the RS cell shows a clear bottom-top asymmetry. A zone of large fluctuations appears where the hot jet impacts the top plate. Then these fluctuations spread along this plate. The cold jet spreads also along the hot plate but with a smaller effect. Moreover, this phenomenon is observable for the vertical velocity fluctuation rms too. These zones of large fluctuations are due to the impact of jets on plates, but this asymmetry could be explained by the difference in plume structure or distribution: More intense and/or more numerous plumes starting from the rough plate could be an explanation for this asymmetry. However, given the intensity of the asymmetry, experimental errors cannot be blamed. Indeed, the rms velocity fluctuation fields remain symmetric in the SS cell.

To make these observations more visible, we plot horizontal velocity fluctuation rms profiles in Fig. 6. For each cell, they are computed by averaging in a horizontal band, 10 cm high, starting from the bottom plate and a similar band starting from the top one. Profiles computed in the bottom region are horizontally flipped on the graph for a better comparison. We observe quantitatively the rise of fluctuations in the presence of roughness. Moreover, the bottom-top asymmetry is very clear and we see fluctuations up to 17% higher in the profile computed at the top of the cell compared to the one computed at the bottom. This confirms observations made on global fields.

C. Velocity structure functions

Since we observed an increase of velocity fluctuations in the presence of roughness, we can wonder if the turbulence structure is modified. In our case we focus on longitudinal structure functions in specific zones of the flow. We choose to calculate these quantities where both the mean

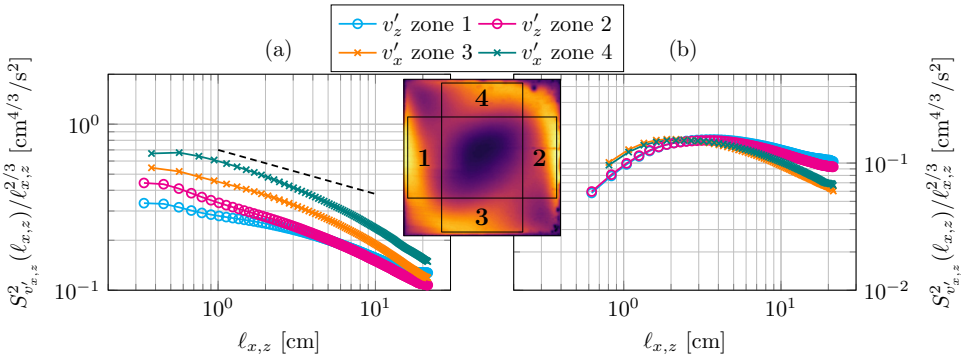

FIG. 7. Comparison of the velocity fluctuations longitudinal structure functions in zones 1–4 in (a) the RS cell and (b) the SS cell. Vertical axes are compensated by $\ell_i^{2/3}$, where $i = x,z$. The dashed line in (a) corresponds to $S^2_{v'_i}(\ell_i) \propto \ell_i^{0.4}$. The inset shows zones where statistics are computed; see the text for the exact box dimensions.

velocity has a constant direction and velocity fluctuations are quite homogeneous. The inset of Fig. 7 shows this cutting. Zones 1 and 2 are 21.5 cm high and 10 cm wide and coincide with cold and hot jets, respectively. Zones 3 and 4 are 10 cm high and 21.5 cm wide. Each zone starts at 1 cm from the boundaries. We define longitudinal second-order structure functions of the velocity fluctuations $(v'_i, i = x,z)$ as

$$\begin{aligned} S^2_{v'_x}(\ell_x) &= \langle [v'_x(x+\ell_x,z,t) - v'_x(x,z,t)]^2 \rangle_{x,z,t}, \\ S^2_{v'_z}(\ell_z) &= \langle [v'_z(x,z+\ell_z,t) - v'_z(x,z,t)]^2 \rangle_{x,z,t}, \end{aligned} \tag{7}$$

where ℓ_x and ℓ_z are the longitudinal spatial increments. In addition, $S^2_{v'_x}$ is computed in zones 3 and 4 and $S^2_{v'_z}$ is computed in zones 1 and 2. According to a numerical study by Kaczorowski *et al.* [24], the structure function calculation in thermal convection is affected by the spatial resolution. They suggest that this resolution must be at least similar to the boundary layer's typical size (1 mm in our case). Unfortunately, we only reach 3 mm in resolution with our PIV measurements. Nevertheless, the global trend of the structure functions is not significantly affected by the resolution in this numerical work [24].

Figures 7(a) and 7(b) show the longitudinal velocity fluctuation structure functions in the different zones for the RS and SS cells respectively. Structure functions are compensated by $\ell_i^{2/3}$, $i = x,z$, to be compared to the well-known Kolmogorov scaling [25,26]

$$S^2_{v'_i} = C_2(\epsilon \ell_i)^{2/3}, \tag{8}$$

where ϵ is the kinetic energy dissipation rate, C_2 is the Kolmogorov constant, and $i = x,z$. For the SS situation we observe a very short plateau for every structure function, which is a signature of a short inertial range with Kolmogorov behavior. To assess the turbulence strength we use the Reynolds number based on the Taylor microscale:

$$R_\lambda = (v^{\mathrm{rms}})^2 \sqrt{\frac{15}{\nu\epsilon}}. \tag{9}$$

We estimate ϵ as [5]

$$\epsilon = \frac{\nu^3}{H^4} \mathrm{Ra}\,\mathrm{Pr}^{-2}(\mathrm{Nu} - 1), \tag{10}$$

which leads to $R_\lambda \approx 35$ for the SS cell and $R_\lambda \approx 60$ for the RS one. Low R_λ makes the inertial range difficult to observe. This explains why the plateaus on compensated SS velocity fluctuation structure

functions are so short. Nevertheless, we can discuss the plateau level linked to the prefactor $C_2\epsilon^{2/3}$ [Eq. (8)]. The top of the compensated structure functions reach about 0.16 ± 0.01 cm$^{4/3}$/s^2. Here C_2 is about constant for $R_\lambda > 100$ ($C_2 \approx 2.1$), but for our Reynolds number we can assess that $C_2 \approx 1.6$ [27]. In the considered zones, it leads to a spatially averaged kinetic energy dissipation rate estimated from velocity structure functions $\epsilon_{SF} = 3.2 \pm 0.4 \times 10^{-2}$ cm^2/s^3. From Eq. (10) the kinetic energy dissipation rate averaged on the whole cell reaches $\epsilon \approx 6.4 \times 10^{-2}$ cm^2/s^3. However, the local value of ϵ is largely inhomogeneous in the flow and depends on the spatial position in the cell, as shown by a numerical study from Kaczorowski *et al.* [24]. They performed their simulations in a rectangular cell with the same vertical and horizontal aspect ratios as our experiment, for Pr = 4.38 and Ra $= 1 \times 10^{10}$. They show that the mean kinetic energy dissipation rate in a parallelepipedic subvolume with dimensions of a quarter of the entire cell in the center of the cell represents only a small percent of the global ϵ computed using Eq. (10). We want to assess quantitatively the kinetic energy dissipation rate in the zones described in the inset of Fig. 7, which are quite far from the cell center. Consequently, we have to use another numerical studyof Kunnen *et al.* [28] performed in a cylindrical geometry, even if the LSC global moves due to this geometry could slightly change the kinetic energy dissipation spatial distribution. Large values of $\epsilon(x,z)$ are observed very close to the boundaries, whereas in the rest of the cell $\epsilon(x,z)$ is up to two orders of magnitude lower. In the zones where we compute the structure functions we voluntarily exclude parts of the flow very close to the boundaries. Using results from Kunnen *et al.* [28] (performed for Pr = 6.4 and Ra $= 1 \times 10^9$), we can estimate that the real averaged $\langle\epsilon(x,z)\rangle_j$ in our zones ($j \in \{1,2,3,4\}$) is between 50% and 70%, the one computed from Eq. (10). Consequently, we obtain $\langle\epsilon(x,z)\rangle_i = 3.8 \pm 0.6 \times 10^{-2}$ cm^2/s^3. We have quite good agreement between $\langle\epsilon(x,z)\rangle_i$ corrected by the inhomogeneity and ϵ_{SF} assessed from $S^2_{v_i}$, $i = x,z$. The small difference could be due to the Ra, Pr, or geometry difference.

While the velocity longitudinal structure functions observed in the SS cell are compatible with the Kolmogorov theory, they differ significantly in the RS cell. A lower scaling appears in zones 2–4, compatible with $\ell_i^{0.4}$, $i = x,z$. In zone 1 the scaling seems slightly higher but does not reach the Kolmogorov one. In this zone plumes from the top smooth plate are dominant, so it is consistent to observe a different scaling from other zones where plumes from the rough plate are dominant, because they are emitted closely (zone 3) or advected (zones 2 and 4). Moreover, we observe that in zone 4, $S^2_{v_x}$ is larger than in zone 3. This is consistent with the bottom-top fluctuation asymmetry observed in the cell (Fig. 4). This difference is less visible in $S^2_{v_z}$ because the zones where it is computed do not capture the asymmetry. This dramatic change of the longitudinal velocity structure functions denotes a large change of the turbulence structure, which does not match with theoretical predictions.

IV. VISCOUS BOUNDARY LAYER STRUCTURE

This dramatic change in the turbulence structure can be linked to the evolution of plume intensity and emission from the hot plate that we observed looking at the fluctuation maps (Figs. 4 and 5). This change of regime could be linked to a change of the boundary layer structure after the transition of the Nu-Ra regime. As pointed in the Introduction, some important changes were observed in the thermal boundary layer in the same cell. We previously showed [17] that the thermal boundary layer above the top of obstacles is thinner than in the case of a smooth plate, which can be linked to a heat flux enhancement. A hypothesis of destabilization of the boundary layers for geometric reasons was proposed to build a model to explain the heat flux increase. This hypothesis was recently confirmed by the study of the viscous boundary layer by PIV in a 6-times-larger proportional cell filled with air at a similar Rayleigh number [18]. A logarithmic layer, the signature of a turbulent boundary layer, was revealed.

In our cell filled with water, it is much more complicated to carry out PIV measurements very close to the roughness. First there are parasite reflections due to particles seeding on the plate. Moreover, intense temperature fluctuations close to the plates lead to large index fluctuations that disturb the visualization. However, the logarithmic layer mentioned before develops quite far enough from the

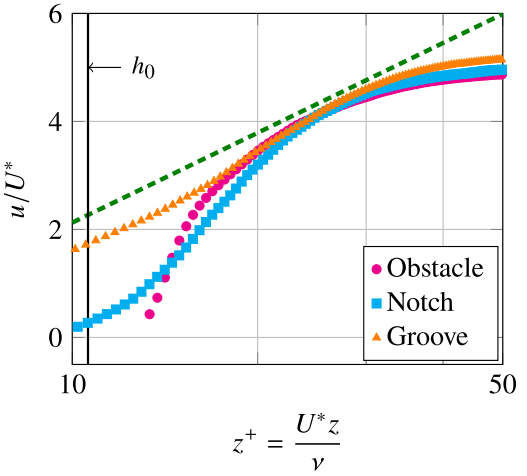

FIG. 8. Horizontal velocity normalized by the function U^* of the normalized altitude z^+ for the three locations (described in Fig. 2). The dashed line represents Eq. (16) for $B = -3.4$. The origin of z is taken at the plate in the groove or notch. Consequently, the obstacle profile starts at h_0. The first points of the profiles are removed because of the lack of resolution very close to the plate.

plate to be observed in the cell. We perform measurements for $\mathrm{Ra} = 4 \times 10^{10}$ (see Table II), which is one order of magnitude higher than the transition Rayleigh number Ra_t. Particle image velocimetry is carried out horizontally centered in the cell (see Fig. 1). We visualize about two obstacles and two notches. To study the shape of the velocity profiles we use the same framework as we previously proposed [18] and commonly employed for logarithmic layers [29]. We estimate a friction velocity using the same method as in a previous similar work [18]. It is defined as

$$\tau = \rho U^{*2}, \tag{11}$$

where ρ is the density of the fluid and τ is the shear stress [29]. This shear stress can be linked to the Reynolds tensor and the velocity gradient

$$\tau = \rho \langle u'v' \rangle_t + \nu \rho \frac{\partial u}{\partial z}, \tag{12}$$

where u' and v' represent the velocity fluctuations of horizontal and vertical velocities, respectively. In the described experiment τ is computed quite far away from the plate, so we can neglect the velocity gradient and

$$U^* \approx \sqrt{\langle u'v' \rangle_t}. \tag{13}$$

Finally, we estimate U^* using the maximum value of the Reynolds tensor

$$U^* = \max(\sqrt{\langle u'v' \rangle_t}). \tag{14}$$

We have $U^* \approx 0.35$ cm/s. Then we define a nondimensional altitude above the rough plate:

$$z^+ = \frac{zU^*}{\nu}. \tag{15}$$

We plot in Fig. 8 the horizontal velocity normalized by U^* in front of z^+ for three locations (above the obstacle, groove, and notch). The resolution of the velocity profiles coupled to a logarithmic scale crushes the region of interest. That is why we plot the profiles only between $z^+ = 10$ and

$z^+ = 50$. They are compared to the logarithmic profile [29]

$$\frac{u}{U^*} = 2.40 \ln z^+ + B, \tag{16}$$

with $B = -3.4$. We observe a short logarithmic layer from $z^+ \approx 20$ particularly visible in the groove. Moreover, the profiles are consistent with the prefactor 2.4. Nevertheless, the estimation of U^* should be considered with care because of the lack of resolution close to the roughness that could affect the adimensionalized profiles. For a smooth plate, the expected constant B is 5.84. In order to know if the surface is hydrodynamically rough, we compare the roughness height h_0 to the viscous sublayer δ, which can be estimated by [30]

$$\delta \approx 5 \frac{\nu}{U^*}. \tag{17}$$

We have $\delta \approx 1.1$ mm, which is smaller than h_0. Consequently, B depends on k^+, defined by

$$k^+ = \frac{h_0 U^*}{\nu}, \tag{18}$$

which reaches about 11 here. The fully rough regime coincides with $k^+ \gg 100$, but a transition regime appears for $k^+ > 5$ [29,30], which is our case. For sand-shape roughness, the experimental values of B in the transition regime are in the range $[-5,5]$. Our observations are consistent with this assertion.

We can now assess the thickness of the thermal boundary layer δ_{th}. This one is expected to be thinner than the viscous sublayer. We adopt the same point of view as our previous study in a rough cell filled with air [18]. An analytical and numerical study by Shishkina *et al.* [31] has shown that the ratio between the thermal and the viscous (δ_v) boundary layers thickness is highly dependent on the attack angle β of the wind on the plate. We extrapolate their results obtained for a laminar boundary layers, so the following discussion should be understood in term of order of magnitude. For a laminar boundary layer the ratio $\delta_{\text{th}}/\delta_v$ ranges from 0.60 ($\beta = \pi/2$) to 1.23 ($\beta = \pi$) for $\text{Pr} = 4.38$. The flow in the logarithmic layer is turbulent, so the attack angle β does not remain constant. If we use this study for our viscous sublayer ($\delta \approx 1.1$ mm), we can only assume that

$$0.66 \text{ mm} \leqslant \delta_\theta \leqslant 1.35 \text{ mm}. \tag{19}$$

Using the model developed by Salort *et al.* [17] in the same cell, the expected thermal boundary layer thickness above an obstacle is 0.64 mm, which is consistent with this estimation for high β.

Finally we find hints of a logarithmic layer above the roughness, in good agreement with experiments carried out in air [18]. It is another clue that in the case of square-stud roughness a turbulent boundary layer could develop above the roughness for Rayleigh numbers higher than Ra_t. This turbulent boundary layer participates fully in the heat flux increase.

V. DISCUSSION AND CONCLUSION

We have observed a large increase of the velocity fluctuations in the presence of roughness compared to two smooth plates. This increase is visible in the whole cell with the appearance of a bottom-top asymmetry and several indications (e.g., the bottom-top velocity fluctuation asymmetry) let us think that it could be attributed to an increase of plumes emission. Moreover, we have confirmed for $\text{Pr} = 4.4$ a possible transition to a turbulent boundary layer close to roughness, as already observed in a proportional configuration and at a similar Ra for $\text{Pr} = 0.7$ [18]. Sharp roughness edges are known to be a source of plume emission as observed at the top of pyramidal roughness [10,11]. However, a turbulent boundary layer could boost the plume emission too, without being discordant with the sharp-edge mechanism. A turbulent boundary layer necessarily implies a logarithmic mean-temperature profile [2,32]. A recent numerical study [33] for $\text{Pr} = 1$ and $\text{Ra} = 5 \times 10^{10}$ has shown that the plume emission regions on a smooth plate correspond to zones of boundary layer where the mean-temperature profile is logarithmic, whereas the location of the plate with no plume

emission does not reveal such a temperature profile. In our case, the wind shear above roughness destabilizes the boundary layer for geometric reasons. Consequently, the boundary layer could transit to turbulence on the whole rough plate, so the plume emission by the bottom plate could be globally increased according to numerical observations cited above [33]. This is consistent with previous background-oriented synthetic schlieren measurements [17] in the same cell, which have shown that the plume emission seems to be homogeneous along the rough plate. Then plumes emitted by the rough plate are advected by the mean wind towards the base of the hot jet and then towards the cold plate, which is why the bottom-top asymmetry is particularly large close to the impacting region of the hot jet (Fig. 4).

Furthermore, the size of thermal plumes could contribute to this elevation of velocity fluctuations. It is usually admitted that their typical size is similar to the thermal boundary layer thickness. Yet the thermal boundary layer is thinner above the roughness than above the top smooth plate [17]. However, the pattern formed by the roughness could have an effect on plume size. One hypothesis is that plumes are emitted either by the top of obstacles or by notches. So they could have a typical size similar to the pattern step (in our case 5 mm), while the smooth thermal boundary layer is about 1 mm. An increase of plume size could be at the origin of the scaling change of velocity structure functions observed between the SS and the RS situations. This assertion is reinforced by the steeper structure function in zone 1 (cold jet) where plumes from the smooth plates, not affected by roughness, are dominant. Unfortunately, we do not have a more precise explanation of this observation.

Finally, the major result of this study is a dramatic increase of velocity fluctuations in the whole cell in the presence of roughness on the bottom plate. This is coupled with a scaling change of the longitudinal velocity structure functions close to the plates and the sidewalls. These observations could be linked to the short logarithmic layer observed above the roughness. Since pointed out by a previous thermometric study [17], the thermal flux measurements in the literature show some discrepancy between the results from different roughness geometries (e.g., pyramidal [10], V-shaped grooves [13], or square studs [16]). The weight of the two mechanisms observed here (the transition to a turbulent boundary layer and plume emission increase) could vary for other square-stud roughness aspect ratios, as it was observed for sinusoidal roughness in recent two-dimensional numerical simulations [34].

ACKNOWLEDGMENTS

We thank Denis Le Tourneau and Marc Moulin for the manufacture of the cell. This study benefited from fruitful discussions and advice from Bernard Castaing. PIV treatments were made possible with the help of PSMN computing resources.

[1] Lord Rayleigh, On convection currents in a horizontal layer of fluid, when the higher temperature is on the under side, Philos. Mag. Ser. 6 **32**, 529 (1916).

[2] R. H. Kraichnan, Turbulent thermal convection at arbitrary Prandtl number, Phys. Fluids **5**, 1374 (1962).

[3] S. Grossmann and D. Lohse, Fluctuations in turbulent Rayleigh-Bénard convection: The role of plumes, Phys. Fluids **16**, 4462 (2004).

[4] F. Chillà and J. Schumacher, New perspectives in turbulent Rayleigh-Bénard convection, Eur. Phys. J. E **35**, 58 (2012).

[5] B. I. Shraiman and E. D. Siggia, Heat transport in high-Rayleigh-number convection, Phys. Rev. A **42**, 3650 (1990).

[6] S. Grossmann and D. Lohse, Scaling in thermal convection: a unifying theory, J. Fluid Mech. **407**, 27 (2000).

[7] G. Ahlers, D. Funfschilling, and E. Bodenschatz, Transitions in heat transport by turbulent convection at Rayleigh numbers up to 10^{15}, New J. Phys. **11**, 123001 (2009).
[8] R. J. A. M. Stevens, E. P. van der Poel, S. Grossmann, and D. Lohse, The unifying theory of scaling in thermal convection: the updated prefactors, J. Fluid Mech. **730**, 295 (2013).
[9] Y. Shen, P. Tong, and K.-Q. Xia, Turbulent Convection Over Rough Surfaces, Phys. Rev. Lett. **76**, 908 (1996).
[10] Y.-B. Du and P. Tong, Turbulent thermal convection in a cell with ordered rough boundaries, J. Fluid Mech. **407**, 57 (2000).
[11] X.-L. Qiu, K.-Q. Xia, and P. Tong, Experimental study of velocity boundary layer near a rough conducting surface in turbulent natural convection, J.Turbul. **6**, N30 (2005).
[12] P. Wei, T.-S. Chan, R. Ni, X.-Z. Zhao, and K.-Q. Xia, Heat transport properties of plates with smooth and rough surfaces in turbulent thermal convection, J. Fluid Mech. **740**, 28 (2014).
[13] P.-E. Roche, B. Castaing, B. Chabaud, and B. Hébral, Observation of the 1/2 power law in Rayleigh-Bénard convection, Phys. Rev. E **63**, 045303 (2001).
[14] G. Stringano, G. Pascazio, and R. Verzicco, Turbulent thermal convection over grooved plates, J. Fluid Mech. **557**, 307 (2006).
[15] S. Ciliberto and C. Laroche, Random Roughness of Boundary Increases the Turbulent Convection Scaling Exponent, Phys. Rev. Lett. **82**, 3998 (1999).
[16] J.-C. Tisserand, M. Creyssels, Y. Gasteuil, H. Pabiou, M. Gibert, B. Castaing, and F. Chillà, Comparison between rough and smooth plates within the same Rayleigh-Bénard cell, Phys. Fluids **23**, 015105 (2011).
[17] J. Salort, O. Liot, E. Rusaouen, F. Seychelles, J.-C. Tisserand, M. Creyssels, B. Castaing, and F. Chill, Thermal boundary layer near roughnesses in turbulent Rayleigh-Bénard convection: Flow structure and multistability, Phys. Fluids **26**, 015112 (2014).
[18] O. Liot, J. Salort, R. Kaiser, R. du Puits, and F. Chillà, Boundary layer structure in a rough Rayleigh-Bénard cell filled with air, J. Fluid Mech. **786**, 275 (2016).
[19] O. Shishkina and C. Wagner, Modelling the influence of wall roughness on heat transfer in thermal convection, J. Fluid Mech. **686**, 568 (2011).
[20] S. Wagner and O. Shishkina, Heat flux enhancement by regular surface roughness in turbulent thermal convection, J. Fluid Mech. **763**, 109 (2015).
[21] G. Ahlers, E. Bodenschatz, D. Funfschilling, S. Grossmann, X. He, D. Lohse, R. J. A. M. Stevens, and R. Verzicco, Logarithmic Temperature Profiles in Turbulent Rayleigh-Bénard Convection, Phys. Rev. Lett. **109**, 114501 (2012).
[22] A. Fincham and G. Delerce, Advanced optimization of correlation imaging velocimetry algorithms, Exp. Fluids **29**, S013 (2000).
[23] K.-Q. Xia, C. Sun, and S.-Q. Zhou, Particle image velocimetry measurement of the velocity field in turbulent thermal convection, Phys. Rev. E **68**, 066303 (2003).
[24] M. Kaczorowski, K.-L. Chong, and K.-Q. Xia, Turbulent flow in the bulk of Rayleigh-Bénard convection: Aspect-ratio dependence of the small-scale properties, J. Fluid Mech. **747**, 73 (2014).
[25] A. N. Kolmogorov, The local structure of turbulence in incompressible viscous fluid for very large Reynolds numbers, Dokl. Akad. Nauk SSSR **30**, 299 (1941).
[26] A. S. Monin and A. M. Yaglom, *Statistical Fluid Mechanics: Mechanics of Turbulence* (Dover, New York, 2007).
[27] K. R. Sreenivasan, On the universality of the Kolmogorov constant, Phys. Fluids **7**, 2778 (1995).
[28] R. P. J. Kunnen, H. J. H. Clercx, B. J. Geurts, L. J. A. van Bokhoven, R. A. D. Akkermans, and R. Verzicco, Numerical and experimental investigation of structure-function scaling in turbulent Rayleigh-Bénard convection, Phys. Rev. E **77**, 016302 (2008).
[29] H. Schlichting and K. Gersten, *Boundary-Layer Theory* (Springer Science & Business Media, New York, 2000).
[30] H. Tennekes and J. L. Lumley, *A First Course in Turbulence* (MIT Press, Cambridge, 1987).
[31] O. Shishkina, S. Horn, and S. Wagner, Falkner-Skan boundary layer approximation in Rayleigh-Bénard convection, J. Fluid Mech. **730**, 442 (2013).

[32] S. Grossmann and D. Lohse, Logarithmic temperature profiles in the ultimate regime of thermal convection, Phys. Fluids **24**, 125103 (2012).

[33] E. P. van der Poel, R. Ostilla-Mónico, R. Verzicco, S. Grossmann, and D. Lohse, Logarithmic Mean Temperature Profiles and Their Connection to Plume Emissions in Turbulent Rayleigh-Bénard Convection, Phys. Rev. Lett. **115**, 154501 (2015).

[34] S. Toppaladoddi, S. Succi, and J. S. Wettlaufer, Roughness as a Route to the Ultimate Regime of Thermal Convection, Phys. Rev. Lett. **118**, 074503 (2017).